

Resonant exciton transfer in mixed-dimensional heterostructures for overcoming dimensional restrictions in optical processes

Received: 21 August 2023

Accepted: 24 November 2023

Published online: 09 December 2023

 Check for updates

N. Fang¹  , Y. R. Chang¹ , D. Yamashita^{2,3}, S. Fujii^{2,4} , M. Maruyama⁵ , Y. Gao⁵ , C. F. Fong¹ , K. Otsuka^{1,6} , K. Nagashio⁷ , S. Okada⁵  & Y. K. Kato^{1,2}  

Nanomaterials exhibit unique optical phenomena, in particular excitonic quantum processes occurring at room temperature. The low dimensionality, however, imposes strict requirements for conventional optical excitation, and an approach for bypassing such restrictions is desirable. Here we report on exciton transfer in carbon-nanotube/tungsten-diselenide heterostructures, where band alignment can be systematically varied. The mixed-dimensional heterostructures display a pronounced exciton reservoir effect where the longer-lifetime excitons within the two-dimensional semiconductor are funneled into carbon nanotubes through diffusion. This new excitation pathway presents several advantages, including larger absorption areas, broadband spectral response, and polarization-independent efficiency. When band alignment is resonant, we observe substantially more efficient excitation via tungsten diselenide compared to direct excitation of the nanotube. We further demonstrate simultaneous bright emission from an array of carbon nanotubes with varied chiralities and orientations. Our findings show the potential of mixed-dimensional heterostructures and band alignment engineering for energy harvesting and quantum applications through exciton manipulation.

The emergence of low-dimensional materials, encompassing one-dimensional (1D) carbon nanotubes (CNTs) and two-dimensional (2D) transition metal dichalcogenides (TMDs), has resulted in the discovery of unique physical phenomena not seen in bulk materials^{1–4}. The reduced screening of Coulomb interactions in these materials leads to tightly bound excitons consisting of electron-hole pairs that remain stable at room temperature, playing a central role in optical processes^{5–8}. In CNTs, the 1D electronic structure gives rise to van Hove

singularities within the density of states, consequently forming discrete excitonic transitions. The resultant excitons are robustly confined within the 1D channel, exhibiting small Bohr radii⁹, short excitonic radiative lifetimes¹⁰, extended diffusion lengths¹¹, efficient exciton-exciton annihilation¹², and single-photon emission at room temperature¹³.

While CNTs offer many intriguing luminescence properties due to their 1D nature, this dimensionality also imposes strict limitations on

¹Nanoscale Quantum Photonics Laboratory, RIKEN Cluster for Pioneering Research, Saitama 351-0198, Japan. ²Quantum Optoelectronics Research Team, RIKEN Center for Advanced Photonics, Saitama 351-0198, Japan. ³Platform Photonics Research Center, National Institute of Advanced Industrial Science and Technology (AIST), Ibaraki 305-8568, Japan. ⁴Department of Physics, Keio University, Yokohama 223-8522, Japan. ⁵Department of Physics, University of Tsukuba, Ibaraki 305-8571, Japan. ⁶Department of Mechanical Engineering, The University of Tokyo, Tokyo 113-8656, Japan. ⁷Department of Materials Engineering, The University of Tokyo, Tokyo 113-8656, Japan. ✉ e-mail: nan.fang@riken.jp; yuichiro.kato@riken.jp

the optical excitation process. Spatially, the diameter of a single-walled CNT is ~ 1 nm, which is considerably smaller than the diffraction-limited diameter of $\sim 1 \mu\text{m}$ for incident laser light. This pronounced size difference restricts the interaction area between CNTs and light, inherently leading to a limited number of photons absorbed¹⁴. Spectrally, the isolated E_{11} and E_{22} transitions in the absorption spectrum necessitate wavelength-tunable lasers to excite CNTs of the desired chirality¹⁵. Furthermore, the 1D confinement of excitons in CNTs results in nearly perfect linear excitation polarization dependence, requiring the polarization angle to be aligned with the nanotube axis¹⁶.

These limitations can be largely mitigated in higher-dimensional materials, such as 2D materials¹⁷. A much more efficient process, therefore, would involve connecting excitation in 2D materials with emission from 1D CNTs via exciton transfer, a phenomenon frequently observed in molecular complexes, biological systems, and semiconductor heterostructures^{18–21}. High-quality interface needed for efficient coupling can be constructed by taking advantage of the van der Waals nature, as the 1D and 2D materials can be stacked together to form mixed-dimensional heterostructures without any lattice matching constraints^{22,23}. With the ideal van der Waals interface, the band alignment in the heterostructure should be mainly governed by the band structure of each individual material rather than the interface, as is the case in the Anderson model^{24,25}. The chirality-dependent bandgap of CNTs thus introduces an important degree of freedom into this system to engineer the band alignment, potentially enabling effective modulation of the exciton transfer process.

Here we investigate the exciton transfer process in CNT/tungsten diselenide (WSe_2) mixed-dimensional heterostructures. Compared with conventional E_{22} excitation in CNTs, the WSe_2 -based excitation offers an immensely larger absorption area, broader spectral response, and polarization-independent efficiency, all of which stem from the 2D nature of the material. Following an extensive exploration of CNT chirality and WSe_2 layer number combinations, we observe that the

exciton transfer efficiency can be significantly modulated due to band alignment. The transfer process shows a resonant behavior, leading to a pronounced enhancement in excitation with fast transfer from the WSe_2 exciton states. Employing this unique excitation process, we demonstrate simultaneous bright emission from an array of CNTs with varied chiralities and orientations. These findings highlight exciton harvesting using mixed-dimensional heterostructures as a novel approach for overcoming the dimensional limitations in optical processes.

Results

Exciton transfer in mixed-dimensional heterostructures

We begin by studying mixed-dimensional heterostructures consisting of a 2D material flake on top of an individual air-suspended CNT. The CNTs are grown over trenches by chemical vapor deposition. For the 2D material, WSe_2 is selected owing to its high stability at room temperature and a large bandgap that could offer sufficiently high energy excitons for transferring into CNTs. A WSe_2 flake is placed on top of the tubes by utilizing the anthracene-assisted transfer technique^{26,27}. The CNT/ WSe_2 heterostructures are therefore entirely free-standing as depicted in Fig. 1a, b, which eliminates the substrate-induced inhomogeneity and dielectric screening effects^{28,29}. The morphology of the heterostructure is examined with an atomic force microscope (Supplementary Fig. 1), and an intimate contact between the CNT and the WSe_2 is confirmed.

Photoluminescence excitation (PLE) spectroscopy can provide evidence for the exciton transfer process. We first focus on a CNT with chirality $(n, m) = (9, 8)$ as an example. Figure 1c shows a PLE map from a pristine suspended $(9, 8)$ CNT before the transfer, with single main peaks for each of the excitation and emission energies corresponding to E_{22} and E_{11} transitions, respectively¹². After transferring a monolayer WSe_2 flake, PL is still bright with 77% of the intensity before the transfer (Fig. 1d). Both E_{11} and E_{22} peaks show redshifts of 33 and 54 meV,

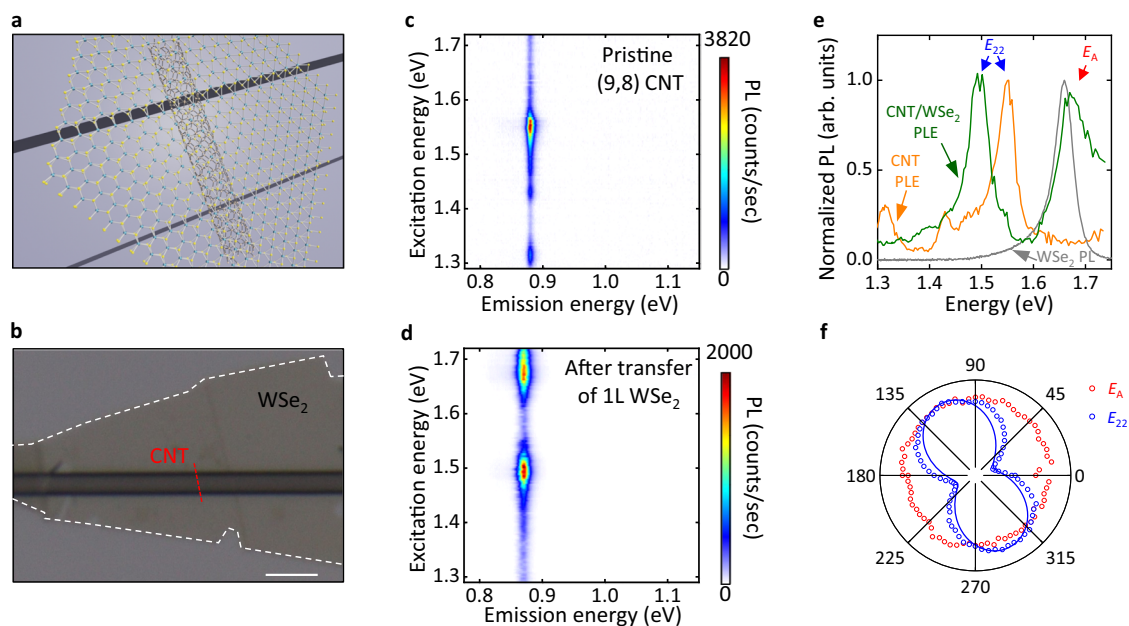


Fig. 1 | Signature of exciton transfer in a 1D-2D heterostructure. **a** A schematic of a suspended CNT/ WSe_2 heterostructure. **b** An optical microscope image of the $(9,8)$ CNT/ 1L WSe_2 heterostructure. The substrate is SiO_2/Si . The scale bar is $5 \mu\text{m}$. **c, d** PLE maps of the $(9,8)$ CNT before (**c**) and after (**d**) the transfer of the 1L WSe_2 . The excitation power is $10 \mu\text{W}$ and the excitation polarization is aligned to CNT axis. **e** Normalized PLE spectra of integrated E_{11} emission for the pristine $(9,8)$ CNT (orange) and after the transfer of 1L WSe_2 (green), and a PL spectrum taken from the

suspended 1L WSe_2 region away from the nanotube in the same sample (gray). The PL spectrum is normalized to the E_A peak. **f** Excitation polarization dependence for E_A excitation (1.676 eV, red circles) and E_{22} excitation (1.521 eV, blue circles). PL emission is plotted as a function of angle with respect to the trench, where 0 degrees correspond to the direction along the trench. The excitation power is $10 \mu\text{W}$. The blue line is a fit to a cosine squared function.

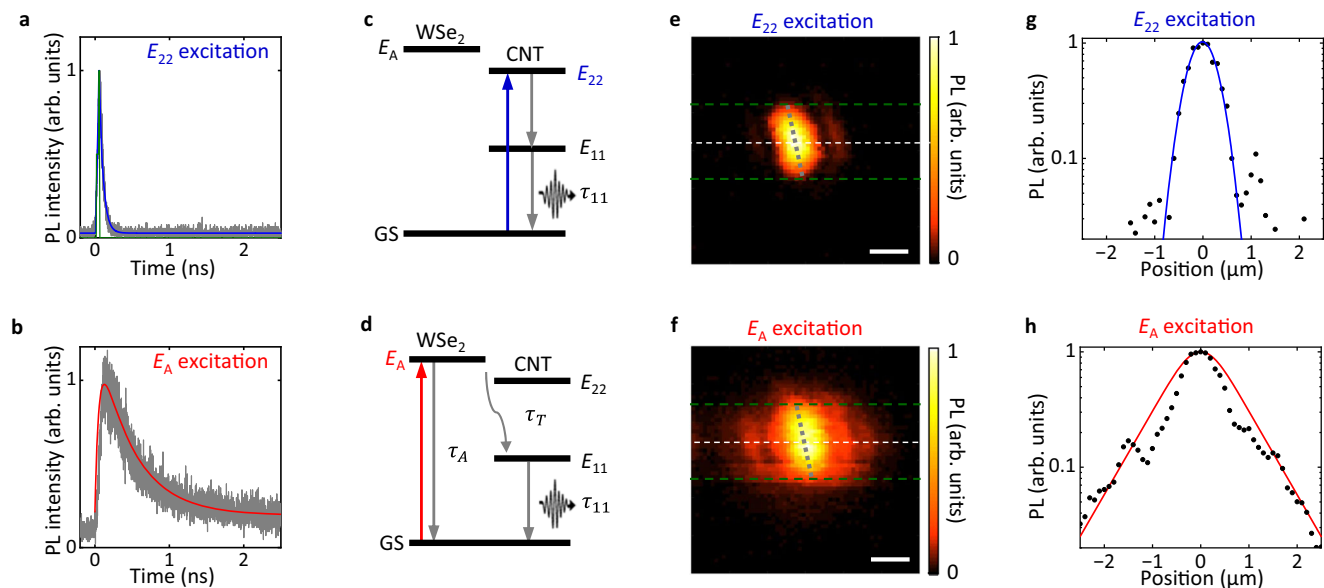


Fig. 2 | Exciton reservoir effect in 1D-2D heterostructures. **a, b** PL decay curves taken from the (9,8) CNT/4L WSe₂ heterostructure at E_{22} (1.494 eV, **a**) and E_A excitation (1.653 eV, **b**). Experimental results and IRF are indicated by gray lines and green lines, respectively. Blue and red lines are fits as explained in the text. **c, d** Energy level diagrams showing the exciton dynamics for E_{22} (**c**) and E_A excitation (**d**). GS indicates the ground state. **e, f** Normalized PL intensity maps from the (9,8) CNT/1L WSe₂ heterostructure at E_{22} (1.494 eV, **e**) and E_A excitation (1.653 eV, **f**).

The PL images are constructed by integrating PL emission over a 30-meV-wide spectral window centered at the E_{11} energy. The trench is indicated by the green broken lines and the CNTs are indicated by the broken gray lines. The scale bar is 1 μm . **g, h** Line profiles from the normalized PL intensity maps indicated by white broken lines in (**e**), (**f**), respectively. Black dots are experimental results and lines are fits. The excitation power is 20 nW for (**a, b**) and 10 μW for (**e, f**).

respectively, arising from substantial dielectric screening effect of WSe₂²³. Remarkably, a prominent high-energy peak appears at -1.673 eV in the excitation dependence.

The origin of the peak can be identified by comparing the PLE spectrum of the heterostructure with the PL spectrum of the suspended WSe₂ (Fig. 1e). The PL spectrum (gray curve) shows a single peak from the A excitons, which overlaps with the newly appeared peak in the PLE spectrum of the heterostructure (green curve). The new peak is therefore denoted as E_A , indicating a process where absorption by WSe₂ A excitons results in emission from CNT E_{11} state. We hypothesize that the exciton transfer process is responsible for coupling the excited and the ground states within different materials. The E_A peak and the E_{22} peak in the PLE spectra (green curve) are comparable in their height, showing that the exciton transfer process is highly efficient despite the different dimensionalities. We also note that the E_A peak in the PLE spectrum shows a considerable tail on the high energy side, which can be explained by the continuum of absorption in WSe₂ arising from interband transitions³⁰.

Excitation polarization measurements offer insights into the dimensionality characteristics of the different excitation pathways. A strong linear polarization dependence emerges from the E_{22} excitation peak as shown in Fig. 1f, consistent with the 1D nature of E_{22} excitons. Conversely, the E_A excitation peak does not display a discernible linear polarization, thereby reflecting the 2D nature of A excitons. This notable polarization distinction enables selective excitation of the samples, either by the A exciton or the E_{22} exciton (Supplementary Fig. 2), thus introducing an additional degree of freedom for excitation manipulation.

Similar exciton transfer processes are observed for heterostructures with thin WSe₂ layers, varying from monolayer (1L) to quad-layer (4L). However, this process is substantially less pronounced in WSe₂ flakes with a thickness of approximately 10 nm (Supplementary Fig. 3). For subsequent analysis, we therefore concentrate primarily on few-layer WSe₂ samples from 1L to 4L.

Exciton reservoir effect in mixed-dimensional heterostructures

Having identified the exciton transfer process in CNT/WSe₂ heterostructures, we carry out time-resolved PL measurements to explore the dynamics of the exciton transfer. A (9,8) CNT/4L WSe₂ heterostructure is investigated by comparing the time-resolved PL signals from E_{11} peaks under two distinct excitation conditions.

For E_{22} excitation, a rapid decay curve is observed (Fig. 2a). We extract the decay lifetime as 52 ps using exponential fitting convoluted with the instrument response function (IRF). This small value is consistent with the bright exciton lifetime for suspended (9,8) CNTs³¹. Interestingly, when under E_A excitation, a much slower decay curve is observed (Fig. 2b).

The marked change in the decay time cannot be ascribed to the increase of E_{11} lifetime since no obvious excitation dependence in E_{11} excitons is observed in terms of spectral peak energy and linewidth. Instead, it can be understood by considering the exciton transfer dynamics, which include WSe₂ A exciton generation, recombination, and transfer processes (Fig. 2c, d).

In the case of E_{22} excitation, given that the relaxation time from E_{22} to E_{11} excitons is on the order of femtoseconds³¹, the rate equation for E_{11} exciton population n_{11} is expressed as

$$\frac{dn_{11}}{dt} = G - \frac{n_{11}}{\tau_{11}}, \quad (1)$$

where G represents generation rate by the laser, and $\tau_{11} = 52$ ps is the lifetime of E_{11} excitons. When excited at the E_A peak, the rate equation for n_{11} is expressed as

$$\frac{dn_{11}}{dt} = \frac{Qn_A}{\tau_T} - \frac{n_{11}}{\tau_{11}}, \quad (2)$$

where Q is the fraction of A excitons interacting with the CNT relative to the total A exciton population n_A , and τ_T represents the transfer time. It is worth noting that the rise time in Fig. 2b is as short as that in

Fig. 2a and below the resolution limited by IRF, indicating that the transfer is a fast process.

The rate equation for n_A in the WSe₂ flake can be represented as

$$\frac{dn_A}{dt} = G - \frac{(1-Q)n_A}{\tau_A} - \frac{Qn_A}{\tau_T}, \quad (3)$$

where τ_A is the A exciton lifetime. In Eq. (3), we consider Q to be negligibly small as only a small portion of A excitons are transferred due to the higher dimensionality of WSe₂. The solution to Eq. (3) is therefore proportional to $\exp(-t/\tau_A)$, and we can accurately reproduce the time-resolved PL in Fig. 2b by setting $\tau_A = 500$ ps and solving Eq. (2). The A exciton lifetime extracted is one order of magnitude larger than that in CNTs (52 ps) as expected from the smaller binding energy, and consistent with previously reported values from mechanically exfoliated WSe₂³². Essentially, the WSe₂ flake serves as an exciton reservoir, continuously supplying excitons to CNTs which leads to the slow decay curve. We note that a smaller τ_A of ~200 ps is observed in the case of a thinner WSe₂ bilayer (Supplementary Fig. 4).

The exciton reservoir effect is also apparent in imaging measurements. We use a three-dimensional motorized stage to scan the (9,8) CNT/1L WSe₂ sample shown in Fig. 1 for obtaining PL images. Since the collection spot is much larger than the excitation spot, emission outside the excitation laser is also collected while the image resolution is determined by the laser spot size. The images therefore represent excitation efficiency profiles for CNT PL, which can be used to identify non-local excitation processes. Figure 2e displays a PL excitation image with the excitation at the E_{22} peak, presenting a typical suspended CNT image with the length of the bright PL area constrained by the trench and the width determined by the Gaussian laser profile. Notably, the PL excitation image for E_A excitation appears spatially expanded, as shown in Fig. 2f. This enlarged PL image indicates that A excitons excited at a distance also funnel into the CNT after diffusion. The WSe₂ flake therefore also acts as a spatial reservoir for exciting CNTs. We also note that the image enlargement occurs not only in the suspended region but also on the substrate, indicating that A excitons are more resilient to substrate effects than E_{11} excitons.

Line profiles of the PL images along the trench for E_{22} and E_A excitation are illustrated in Fig. 2g and h, respectively. The E_{22} -excited profile is fitted using a Gaussian function, yielding a $1/e^2$ radius of the laser spot $r = 0.58 \mu\text{m}$. For the E_A excitation, the PL intensity is proportional to the density of A exciton transferred to the CNT position, assuming that the exciton transfer is a linear process. The line profile at E_A excitation is hence fitted to a solution of a steady-state one-dimensional diffusion equation

$$D \frac{d^2 n_A(x)}{dx^2} - \frac{n_A(x)}{\tau_A} + \frac{G}{\sqrt{2\pi}r^2} e^{-2x^2/r^2} = 0, \quad (4)$$

where x is the position along the trench direction and D is the diffusion coefficient. Given $r = 0.58 \mu\text{m}$, the simulated profile with a diffusion length $L = \sqrt{D\tau_A} = 0.60 \mu\text{m}$ matches the experimental data as shown in Fig. 2h. The diffusion lengths are also estimated for heterostructures with thicker WSe₂ flakes, reaching up to $1.10 \mu\text{m}$ (Supplementary Fig. 5). It is worth mentioning that the diffusion length here is larger than previously reported values³³, possibly due to the suspended structure of the WSe₂ flake which has reduced scattering sites.

Band alignment tuning and resonant exciton transfer

The efficient exciton reservoir effect observed in both spatial and temporal domains suggests the possibility of a greatly enhanced exciton transfer under suitable band alignment. To explore the optimized structure, we take advantage of the variable bandgap of CNT with chirality. We have fabricated 34 CNT/WSe₂ heterostructures using

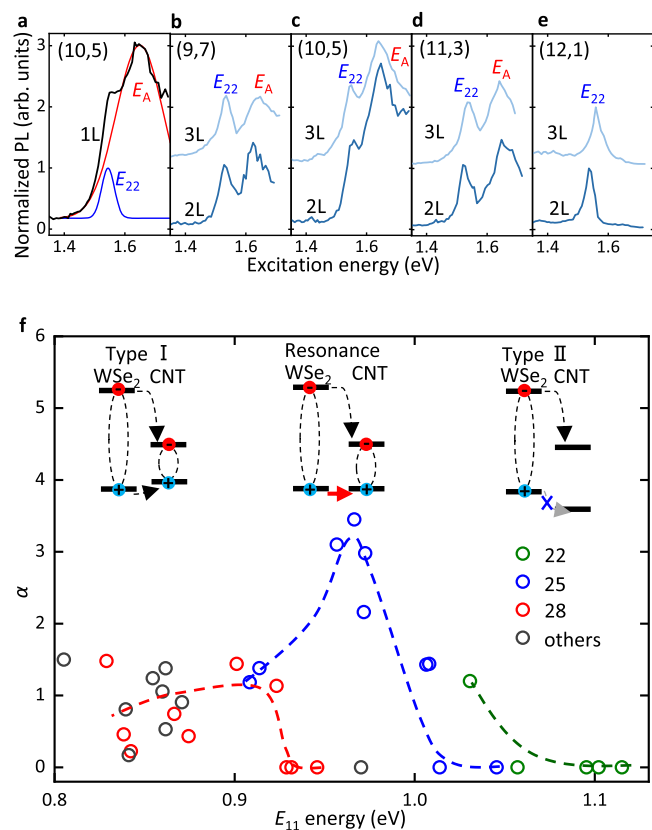


Fig. 3 | Band alignment tuning and resonant exciton transfer. **a–e** Normalized PLE spectra of integrated E_{11} emission for the (10,5) CNT/1L WSe₂ sample (**a**), (9,7) CNT/2L and 3L WSe₂ samples (**b**), (10,5) CNT/2L and 3L WSe₂ samples (**c**), (11,3) CNT/2L and 3L WSe₂ samples (**d**), (12,1) CNT/2L and 3L WSe₂ samples (**e**). The PLE spectra are normalized to the E_{22} peak intensity. In (**b–e**), baselines of PLE spectra for the samples with 2L and 3L WSe₂ are 0 and 1, respectively. The excitation power is $10 \mu\text{W}$. **f** Factor α as a function of E_{11} energy from all samples. CNT families of 22, 25, 28, and others are indicated by green, blue, red, and gray circles, respectively. Broken lines are guide to the eye. (Inset) Schematics of band alignment of CNT/WSe₂ heterostructures. With varying CNT chirality, the band alignment transition from type-I to type-II occurs. Black arrows indicate the exciton tunneling process, while a red arrow indicates the resonant tunneling of holes when the valence bands match.

17 different chiralities (see Supplementary Table 1 for the list of samples) and have quantitatively characterized the exciton transfer process.

Figure 3a displays the PLE spectrum from a (10,5) CNT/1L WSe₂ heterostructure, which has demonstrated the largest enhancement of the exciton transfer. The E_A peak is dominating the spectrum, and the E_{22} peak is almost overwhelmed. Gaussian peak fits are carried out to distinguish the two excitation peaks. The efficiency factor $\alpha = I(E_A)/I(E_{22})$ is defined to quantify the E_A excitation process with respect to the E_{22} excitation, where $I(E_A)$ and $I(E_{22})$ are the peak intensities of E_A and E_{22} , respectively. In this heterostructure, the exciton population is multiplied by $\alpha = 3.5$ compared with E_{22} excitation. Under such an effective excitation through A excitons, we note that the exciton-exciton annihilation (EEA) process¹² is strong and the α factor is underestimated. A PLE measurement at a low laser power to avoid the EEA effect leads to an increased α factor of 6.2 (see Supplementary Fig. 6). From the α factor, we estimate that approximately 3.8% of the A excitons transfer into the nanotube, taking into account the different absorption areas and absorption coefficients (see Supplementary Note 8). While this value may not seem high, it is actually substantial because the exciton population in WSe₂ is orders of magnitude larger than in CNTs.

To elucidate the origin of the enhanced transfer, we plot the PLE spectra for the heterostructures with bilayer (2L) and trilayer (3L) WSe₂ transferred onto CNTs with varying chiralities of (9,7), (10,5), (11,3), and (12,1) in Fig. 3b–e, respectively. The selected chiralities here belong to the same family ($2n + m = 25$). The PLE spectra from (9,7) and (11,3) samples exhibit clear E_A peaks, although weaker than that in (10,5) CNTs. In contrast, the E_A peak is unresolved in (12,1) samples, indicating a strong suppression of the exciton transfer process.

The observed chirality-dependent exciton transfer processes cannot be explained by the commonly observed Förster-type energy transfer in 2D heterostructures^{34,35}. For the energy transfer process where WSe₂ A exciton is the donor and CNT E_{22} exciton is the acceptor, we do not expect changes in the transfer efficiency unless the spectral overlap is modulated substantially. The chiralities shown in Fig. 3b–e have similar E_{22} energies but exhibit large changes in the efficiency factors, inconsistent with Förster-type energy transfer.

Instead, we interpret our data with a direct exciton tunneling process, which should be sensitive to the band alignment between the two materials^{36,37}. For CNT/2L WSe₂ samples, the E_{11} energies for chiralities of (9,7), (10,5), (11,3), and (12,1) are 0.914, 0.973, 1.008, and 1.046 eV, respectively. Since the E_{11} energy reflects the bandgap of CNTs, the band alignment should be varied, as illustrated in Fig. 3f. For chiralities with smaller bandgap, type-I heterojunction is expected where exciton tunneling is allowed. As the bandgap gets larger, the valence band offset between CNT and WSe₂ becomes smaller. When the bands match, we expect resonant tunneling for the holes, and this maybe the case for (10,5) CNTs with significantly enhanced E_A excitation peak. With further increase in the bandgap, transition to type-II heterojunction should occur. The exciton transfer would then become inhibited due to the barrier for the hole tunneling, which is consistent with the PLE spectra for (12,1).

We perform density functional theory studies to examine the band alignment within the heterostructure (Supplementary Fig. 7). Results show that offsets in the valence band is less significant than that in the conduction band. The variation of chirality from lower E_{11} energy to a higher one ultimately instigates the reversal of the valence band offset, thus leading to the transition from type-I to type-II. The

theoretical findings corroborate with the empirical results described above, supporting the picture that band alignment transition is taking place and confirming the exciton transfer process.

The transition is more clearly observed by plotting the α factor against the E_{11} energy, as shown in Fig. 3f. For family number 25, the resonant peak can be seen at E_{11} energy around 0.97 eV. The band alignment transitions are consistently observed for families 22 and 28 with the threshold E_{11} energy of the transition increasing with the family number. The CNT families, recognized for impacting the band structure of CNTs via trigonal warping and curvature effects³⁸, may also be influencing the band alignment in the heterostructures here. It should be noted that there is no observable resonance in families 22 and 28, which could be attributed to the absence of a chirality with an exactly matched band energy.

The highly efficient exciton transfer at the resonance suggests it is a rapid process, and we perform Monte Carlo simulations to gain more insight. Exciton generation, diffusion, transfer, and recombination processes are included, and we find the transfer time $\tau_T = 1.1$ ps reproduce the experimental value of $\alpha = 6.2$ (see Supplementary Note 8). In contrast, mixed-dimensional heterostructures consisting of zero-dimensional quantum dots and 2D TMDs show a long exciton transfer time in the range of 1–10 ns^{39,40}. Such a long transfer time is primarily caused by complex interfaces consisting of shells and ligands. The transfer process observed in this study is remarkably fast and comparable with homogeneous dimensional structures, such as 2D-2D TMD and 1D-1D CNT heterostructures^{34,41}. The rapid transfer process can be ascribed to the intimate contact between the CNT and WSe₂, facilitated by the uniform van der Waals interface and the presence of a resonant tunneling condition.

Overcoming the dimensional restrictions on excitation in a CNT array/WSe₂ heterostructure

With relaxed optical selection rules and pronounced exciton reservoir effects, the A exciton based excitation has a more distinct effect on an array of CNTs. The array under investigation comprises of four tubes located from left to right with chiralities of (8,7), (9,8), (10,5), and (10,5), and is covered by a monolayer flake. Figure 4a shows a PL

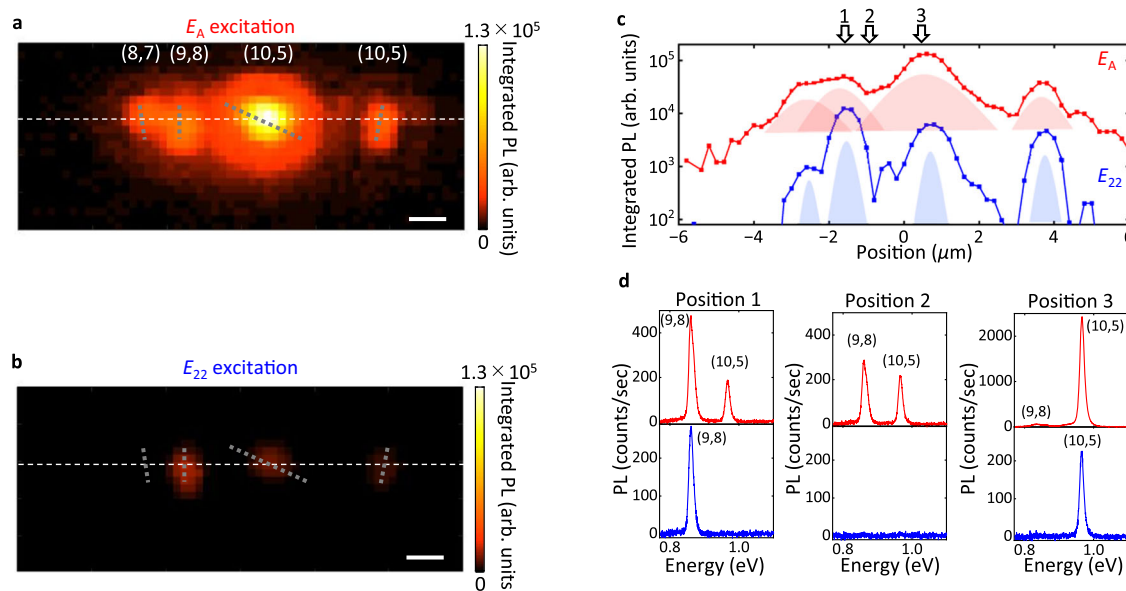


Fig. 4 | Simultaneous excitation of a CNT array in a mixed-dimensional heterostructure. **a, b** PL intensity maps for E_A (1.664 eV, **a**) and E_{22} (1.494 eV, **b**) excitation. The PL images are constructed by integrating the full PL spectrum. The CNT chiralities are (8,7), (9,8), (10,5), and (10,5) from left to right, and the positions and orientations are indicated by the broken gray lines. The scale bar is 1 μm . **c** Line

profiles indicated by white broken lines in **(a)**, red and **(b)**, blue. **d** PL spectra taken at Positions 1, 2, and 3 as indicated in **(c)**. The upper three PL spectra are taken with E_A excitation and the bottom three PL spectra are taken with E_{22} excitation. The excitation power is 3 μW .

excitation image with E_A excitation, whereas Fig. 4b is an excitation image taken with E_{22} excitation for the (9,8) tube. The excitation at the E_A energy results in high intensity PL from all tubes and a quasi-2D excitation image spanning the trench. We note that the two (10,5) CNTs exhibit different PL intensities, which is primarily due to their different lengths¹². The line profile (Fig. 4c, red) shows spatially continuous emission over 10 μm , resulting from overlapping tube images enlarged by exciton diffusion. In comparison, tube images are completely isolated in Fig. 4b and its line profile (Fig. 4c, blue). Furthermore, the (8,7) tube is unnoticeable since the excitation energy is detuned from its E_{22} energy and the polarization angle is misaligned. In general, achieving simultaneous excitation across all tubes remains a challenge due to different E_{22} energies and varying angles amongst the CNTs.

The diffusion process can be over one micron (Supplementary Fig. 5), allowing for enhanced versatility in exciting multiple tubes. In Fig. 4d, we plot PL spectra at three representative positions for E_A excitation (red) and E_{22} excitation (blue). Simultaneous PL emission from spatially distant (9,8) and (10,5) tubes is demonstrated by E_A excitation at the region in between (Position 2, red). In contrast, no PL is observed under E_{22} excitation at this position (blue).

Discussion

In conclusion, an efficient exciton transfer process within CNT/WSe₂ heterostructures has been observed. Excitation via WSe₂ A excitons presents several distinctive features compared to traditional E_{22} excitation: larger absorption areas, broader spectra, and tolerance to polarization misalignment. Through the examination of 17 different CNT chiralities, it has been confirmed that the exciton transfer is significantly modulated by the band alignment. The (10,5) CNT/WSe₂ heterostructure demonstrates the resonant exciton transfer, leading to a considerable enhancement of E_A excitation efficiency and a rapid transfer time of 1.1 ps. The ability to simultaneously illuminate CNT arrays of varying chiralities and orientations, resulting in a quasi-2D image under E_A excitation, is also demonstrated. These observations propose that the exciton transfer process in mixed-dimensional heterostructures could be harnessed for generation of excitons in CNTs, thus providing a promising avenue to surpass the excitation constraints in low-dimensional materials. The high tunability of the band alignment indicates the potential for more intriguing excitons to emerge in this system, for example, indirect excitonic states at the mixed-dimensional interface under type-II band alignment.

Methods

Air-suspended carbon nanotube growth

In preparing air-suspended CNTs, we utilize silicon dioxide (SiO₂)/silicon (Si) substrates with trenches¹². The process begins with patterning of alignment markers and trenches onto the Si substrates, utilizing electron-beam lithography. The trenches, with lengths of approximately 900 μm and widths varying between 0.5 and 3.0 μm , are subsequently formed by dry etching. The substrate is then subjected to thermal oxidation, resulting in the formation of a SiO₂ film inside the trenches, with a thickness typically ranging from 60 to 70 nm. The next step involves a further instance of electron-beam lithography to designate catalyst areas along the trench edges. An iron (Fe) film with a thickness of approximately 1.5 Å is then deposited by an electron beam evaporator, serving as a catalyst in the CNT growth. The final step of the process is the synthesis of CNTs, achieved through alcohol chemical vapor deposition at a temperature of 800 °C for 1 min. Optimization of the iron film thickness is crucial in controlling the yield for predominantly producing isolated synthesized CNTs. PLE spectroscopy is conducted to identify the chiralities of suspended CNTs by comparing E_{11} and E_{22} energies to tabulated data¹². In order to form the heterostructures with WSe₂, we specifically select isolated, fully

suspended chirality-identified CNTs with lengths in the range of 0.5 to 2.0 μm .

Anthracene crystal growth

For the purpose of stamping WSe₂ flakes onto CNTs, anthracene crystals are grown through an in-air sublimation process^{26,27}. The procedure commences with the placement of anthracene powder onto a glass slide, which is subsequently heated to 80 °C. A secondary glass slide is positioned above the anthracene source, generally maintaining a 1 mm gap. Following this setup, thin, large-area single crystals begin to grow out of the glass surface. To enhance the growth of thin, large-area crystals, the glass slides are patterned using ink from commercially available markers, effectively inhibiting the nucleation of three-dimensional crystals. The typical growth time for anthracene crystals is 10 h.

WSe₂ transfer using anthracene crystals

WSe₂ crystals are purchased from HQ graphene. Flakes of WSe₂ are prepared on conventional 90-nm-thick SiO₂/Si substrates by employing a mechanical exfoliation technique. Layer number is determined by optical contrast. A polydimethylsiloxane (PDMS) sheet supported by glass is used to collect a single anthracene crystal, creating an anthracene/PDMS stamp. The targeted WSe₂ flakes on the substrate are subsequently picked up by pressing the anthracene/PDMS stamp. Rapid separation of the stamp (>10 mm/s) ensures the adherence of the anthracene crystal to the PDMS sheet. The stamp is then applied to the receiving substrate with the desired chirality-identified CNT, whose position is determined by a prior measurement. Precise position alignment is accomplished with the aid of markers prepared on the substrate. Gradual retraction of the PDMS (<0.2 $\mu\text{m}/\text{s}$) allows for the anthracene crystal carrying the WSe₂ flake to settle on the receiving substrate. The anthracene crystal is then removed via sublimation in air at 110 °C over a 10-min period, leaving a clean suspended CNT/WSe₂ heterostructure. This completely dry process eliminates the risk of contamination from solvent. Moreover, the solid single-crystal anthracene serves to shield the 2D flakes and the CNT throughout the transfer, ensuring that the CNT/WSe₂ heterostructure experiences minimal strain^{26,27}. We note that some of the CNT/WSe₂ samples exhibit substantially small E_{11} and E_{22} energy shifts of less than 5 meV, suggesting a lack of contact between the CNT and the WSe₂. These samples are excluded in the following study.

Photoluminescence measurements

A custom-built confocal microscopy apparatus is utilized to perform PL measurements for CNT E_{11} excitons at ambient temperature within an atmosphere of dry nitrogen gas^{12,23}. A variable wavelength Ti:sapphire laser serves as a continuous-wave excitation source, with its power controlled via neutral density filters. The laser beam is focused onto the samples with an objective lens featuring a numerical aperture of 0.65 and a working distance of 4.5 mm. The $1/e^2$ diameter of the laser spot is 1.16 μm . The confocal pinhole defines the collection spot size, which is approximately 5.4 μm in diameter. A longpass filter with a cut-on wavelength of 1050 nm is used to collect the PL emission from CNTs. PL is gathered through the same objective lens and detected by a liquid-nitrogen-cooled 1024-pixel indium gallium arsenide diode array attached to a spectrometer. A 150-lines/mm grating is used to obtain a dispersion of 0.52 nm/pixel at a wavelength of 1340 nm. PL excitation images are taken by using a three-dimensional motorized stage to scan the CNT/WSe₂ samples in our confocal microscopy system. A PL spectrum is collected at each position, and PL excitation images are constructed by integrating the CNT emission. For photoluminescence measurements of WSe₂ A excitons, a 532-nm laser and a charge-coupled device camera are employed. Polarization is aligned to the tube unless otherwise noted.

Time-resolved measurements

Approximately 100 femtosecond pulses at a repetition rate of 76 MHz from a Ti:sapphire laser is utilized for excitation. The laser beam is directed onto the sample using an objective lens with a numerical aperture of 0.85 and a working distance of 1.48 mm. The PL from the center of the nanotube within the heterostructure is coupled to a superconducting single-photon detector with an optical fiber, and a time-correlated single-photon counting module is used to collect the data. IRFs dependent on the detection wavelength are acquired by dispersing supercontinuum white light pulses with a spectrometer. The experiments are conducted at room temperature in air.

Data availability

All the data generated in this study have been deposited in the R2DMS-GakuNinRDM database at <https://dmsgrdm.riken.jp/sdgab/>. Source data are provided with this paper.

References

1. Ilani, S., Donev, L. A. K., Kindermann, M. & McEuen, P. L. Measurement of the quantum capacitance of interacting electrons in carbon nanotubes. *Nat. Phys.* **2**, 687 (2006).
2. Postma, H. W. C., Teepen, T., Yao, Z., Grifoni, M. & Dekker, C. Carbon nanotube single-electron transistors at room temperature. *Science* **293**, 76 (2001).
3. Wu, W. et al. Piezoelectricity of single-atomic-layer MoS₂ for energy conversion and piezotronics. *Nature* **514**, 470 (2014).
4. Domaretskiy, D. et al. Quenching the bandgap of two-dimensional semiconductors with a perpendicular electric field. *Nat. Nanotechnol.* **17**, 1078 (2022).
5. Wang, F., Dukovic, G., Brus, L. E. & Heinz, T. F. The optical resonances in carbon nanotubes arise from excitons. *Science* **308**, 838 (2005).
6. Jones, A. M. et al. Spin-layer locking effects in optical orientation of exciton spin in bilayer WSe₂. *Nat. Phys.* **10**, 130 (2014).
7. Rivera, P. et al. Valley-polarized exciton dynamics in a 2D semiconductor heterostructure. *Science* **351**, 688 (2016).
8. Wang, Z., Shan, J. & Mak, K. F. Valley- and spin-polarized Landau levels in monolayer WSe₂. *Nat. Nanotechnol.* **12**, 144 (2017).
9. Lüer, L. et al. Size and mobility of excitons in (6, 5) carbon nanotubes. *Nat. Phys.* **5**, 54 (2009).
10. Machiya, H., Yamashita, D., Ishii, A. & Kato, Y. K. Evidence for near-unity radiative quantum efficiency of bright excitons in carbon nanotubes from the Purcell effect. *Phys. Rev. Res.* **4**, 022011 (2022).
11. Ishii, A., Yoshida, M. & Kato, Y. K. High efficiency dark-to-bright exciton conversion in carbon nanotubes. *Phys. Rev. X* **9**, 041048 (2019).
12. Ishii, A., Yoshida, M. & Kato, Y. K. Exciton diffusion, end quenching, and exciton-exciton annihilation in individual air-suspended carbon nanotubes. *Phys. Rev. B* **91**, 125427 (2015).
13. Ishii, A., Yoshida, M. & Kato, Y. K. Room-temperature single-photon emission from micrometer-long air-suspended carbon nanotubes. *Phys. Rev. Appl.* **8**, 054039 (2017).
14. Streit, J. K., Bachilo, S. M., Ghosh, S., Lin, C.-W. & Weisman, R. B. Directly measured optical absorption cross sections for structure-selected single-walled carbon nanotubes. *Nano Lett.* **14**, 1530 (2014).
15. Lefebvre, J. & Finnie, P. Excited excitonic states in single-walled carbon nanotubes. *Nano Lett.* **8**, 1890 (2008).
16. Lefebvre, J. & Finnie, P. Polarized photoluminescence excitation spectroscopy of single-walled carbon nanotubes. *Phys. Rev. Lett.* **98**, 167406 (2007).
17. Kozawa, D. et al. Photocarrier relaxation pathway in two-dimensional semiconducting transition metal dichalcogenides. *Nat. Commun.* **5**, 4543 (2014).
18. Achermann, M. et al. Energy-transfer pumping of semiconductor nanocrystals using an epitaxial quantum well. *Nature* **429**, 642 (2004).
19. Han, J.-H. et al. Exciton antennas and concentrators from core-shell and corrugated carbon nanotube filaments of homogeneous composition. *Nat. Mater.* **9**, 833 (2010).
20. Tabachnyk, M. et al. Resonant energy transfer of triplet excitons from pentacene to PbSe nanocrystals. *Nat. Mater.* **13**, 1033 (2014).
21. Struck, D. K., Hoekstra, D. & Pagano, R. E. Use of resonance energy transfer to monitor membrane fusion. *Biochemistry* **20**, 4093 (1981).
22. Jariwala, D., Marks, T. J. & Hersam, M. C. Mixed-dimensional van der Waals heterostructures. *Nat. Mater.* **16**, 170 (2016).
23. Fang, N. et al. Hexagonal boron nitride as an ideal substrate for carbon nanotube photonics. *ACS Photonics* **7**, 1773 (2020).
24. Davies, F. H., Price, C. J., Taylor, N. T., Davies, S. G. & Hepplestone, S. P. Band alignment of transition metal dichalcogenide heterostructures. *Phys. Rev. B* **103**, 045417 (2021).
25. Chaves, A. et al. Bandgap engineering of two-dimensional semiconductor materials. *npj 2D Mater. Appl.* **4**, 29 (2020).
26. Otsuka, K. et al. Deterministic transfer of optical-quality carbon nanotubes for atomically defined technology. *Nat. Commun.* **12**, 3138 (2021).
27. Fang, N. et al. Quantization of mode shifts in nanocavities integrated with atomically thin sheets. *Adv. Opt. Mater.* **10**, 2200538 (2022).
28. Sun, X. et al. Enhanced interactions of interlayer excitons in free-standing heterobilayers. *Nature* **610**, 478 (2022).
29. Lefebvre, J., Homma, Y. & Finnie, P. Bright band gap photoluminescence from unprocessed single-walled carbon nanotubes. *Phys. Rev. Lett.* **90**, 217401 (2003).
30. Steinleitner, P. et al. Direct observation of ultrafast exciton formation in a monolayer of WSe₂. *Nano Lett.* **17**, 1455 (2017).
31. Manzoni, C. et al. Intersubband exciton relaxation dynamics in single-walled carbon nanotubes. *Phys. Rev. Lett.* **94**, 207401 (2005).
32. Jin, C. et al. On optical dipole moment and radiative recombination lifetime of excitons in WSe₂. *Adv. Funct. Mater.* **27**, 1601741 (2017).
33. Cadiz, F. et al. Exciton diffusion in WSe₂ monolayers embedded in a van der Waals heterostructure. *Appl. Phys. Lett.* **112**, 152106 (2018).
34. Kozawa, D. et al. Evidence for fast interlayer energy transfer in MoSe₂/WS₂ heterostructures. *Nano Lett.* **16**, 4087 (2016).
35. Hu, Z. et al. Trion-mediated Förster resonance energy transfer and optical gating effect in WS₂/hBN/MoSe₂ heterojunction. *ACS Nano* **14**, 13470 (2020).
36. Kavka, J. J., Shegelski, M. R. & Hong, W.-P. Tunneling and reflection of an exciton incident upon a quantum heterostructure barrier. *J. Phys.: Condens. Matter* **24**, 365802 (2012).
37. Huang, Z. et al. Evolution from tunneling to hopping mediated triplet energy transfer from quantum dots to molecules. *J. Am. Chem. Soc.* **142**, 17581 (2020).
38. Jiang, J. et al. Chirality dependence of exciton effects in single-wall carbon nanotubes: Tight-binding model. *Phys. Rev. B* **75**, 035407 (2007).
39. Prins, F., Goodman, A. J. & Tisdale, W. A. Reduced dielectric screening and enhanced energy transfer in single- and few-layer MoS₂. *Nano Lett.* **14**, 6087 (2014).
40. Tanoh, A. O. A. et al. Directed energy transfer from monolayer WS₂ to near-infrared emitting PbS-CdS quantum dots. *ACS Nano* **14**, 15374 (2020).
41. Qian, H. et al. Exciton energy transfer in pairs of single-walled carbon nanotubes. *Nano Lett.* **8**, 1363 (2008).

Acknowledgements

Parts of this study are supported by JSPS (KAKENHI JP22K14624 to D.Y., JP22K14625 to S.F., JP21K14484 to M.M., JP22K14623 to C.F.F., JP21H05233 to S.O., JP22F22350 to Y.R.C., JP23H00262, JP20H02558 to Y.K.K.) and MEXT (ARIM JPMXP1222UT1135). Y.R.C. is supported by JSPS (International Research Fellow). N.F. and C.F.F. are supported by the RIKEN Special Postdoctoral Researcher Program. We thank the Advanced Manufacturing Support Team at RIKEN for technical assistance.

Author contributions

N.F. carried out sample preparation and performed measurements on all the samples. Y.R.C. performed atomic force microscope measurements and assisted in other measurements. D.Y. and S.F. contributed to the time-resolved PL measurements. M. M., Y.G., and S.O. performed density functional theory calculations. Y.R.C., C.F.F., and K.N. assisted in sample preparation. K.O. aided in the development of the anthracene-assisted transfer method. Y.K.K. supervised the project. N.F. and Y.K.K. co-wrote the manuscript, with all authors providing input and comments on the manuscript.

Competing interests

The authors declare no competing interests.

Additional information

Supplementary information The online version contains supplementary material available at <https://doi.org/10.1038/s41467-023-43928-2>.

Correspondence and requests for materials should be addressed to N. Fang or Y. K. Kato.

Peer review information *Nature Communications* thanks the anonymous reviewers for their contribution to the peer review of this work. A peer review file is available.

Reprints and permissions information is available at <http://www.nature.com/reprints>

Publisher's note Springer Nature remains neutral with regard to jurisdictional claims in published maps and institutional affiliations.

Open Access This article is licensed under a Creative Commons Attribution 4.0 International License, which permits use, sharing, adaptation, distribution and reproduction in any medium or format, as long as you give appropriate credit to the original author(s) and the source, provide a link to the Creative Commons license, and indicate if changes were made. The images or other third party material in this article are included in the article's Creative Commons license, unless indicated otherwise in a credit line to the material. If material is not included in the article's Creative Commons license and your intended use is not permitted by statutory regulation or exceeds the permitted use, you will need to obtain permission directly from the copyright holder. To view a copy of this license, visit <http://creativecommons.org/licenses/by/4.0/>.

© The Author(s) 2023